# Development of a Capacitive Temperature Sensor Using a Lead-Free Ferroelectric $Bi(Fe_{2/3}Ta_{1/3})O_3$ Ceramic

Sarbasri Halder, Satyanarayan Bhuyana, *Member, IEEE*, Ashis Tripathy,
Omar Al Zaabi, *Member, IEEE*, Biswaranjan Swain,
and Utkal Ranjan Muduli, *Senior Member, IEEE*

Abstract—Ceramic materials have many striking prospects as temperature sensors. Still, some inevitable shortcomings comprising toxicity, low biocompatibility, extensive response as well as recovery times, poor sensitivity, and hysteresis obstruct them from various progressive uses. Therefore, in this current exploration, a capacitive temperature sensor has been designed and developed using a lead-free ferroelectric ceramic $Bi(Fe_{2/3}Ta_{1/3})O_3$ (BFT) by solid-state sintering technique. Compared with the conventional capacitive temperature sensor, the proposed BFT-based temperature sensor has a relatively high sensitivity of 280 fF/°C, a fast response time (4.27 s), and a recovery time (7.39 s). The developed sensor provides a reversible response with relatively low hysteresis and excellent repeatability over multiple cycles. The sensor's response has been recorded for 30 days to confirm long-term stability. The excellent sensing properties of nontoxic BFT sensors make them a very promising electronic component for the development of high-performance capacitive temperature sensors for advanced electronic applications.

Index Terms— Active low-pass filter (LPF), capacitive temperature sensor, ferroelectric ceramic, relatively low hysteresis, sensitivity.
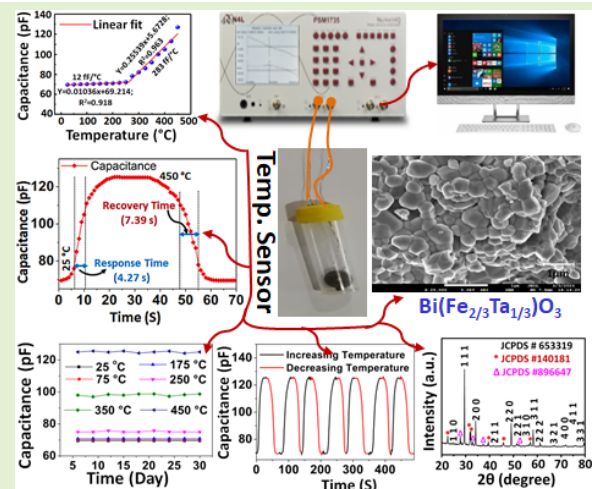
I. INTRODUCTION

IN RECENT years, the research interest of the scientific community has increased considerably for the development of innovative ferroelectric materials [1], [2]. The ferroelectric ceramic materials with improved electrical, mechanical, chemical, and optical characteristics play a significant role in the fabrication of various functional sensor devices [3], [4] that find usage in the monitoring of motion [5], temperature [6], pressure [7], magnetic field [8], and IR radiation [9]. Spontaneous polarization is the key behavior of ferroelectric material which is sensitive to many external stimuli, such as electric and magnetic fields, mechanical deformation, temperature, and pressure. In addition, the pyroelectric characteristic of ferroelectric material makes it suitable for the realization of capacitive temperature sensors [10], [11]. Temperature sensors play a significant character in various sectors, such as the food industry (quality control of food) [12], biomedical (temperature monitoring of the human body, newborn baby incubators, and pharmaceutical quality control) [13], automotive (engine oil and in-out air temperature monitoring), electronics industry (battery life monitoring, cell phone, refrigerator temperature control, and integrated circuits) [14], defense as well as aviation industries (temperature monitoring

in spacecraft, satellite, and physiological monitoring) [15], and meteorological/environmental applications (for weather forecasting) [16].

Researchers across the globe are trying to alter various sensor characteristics, such as capacitance, dielectric constant, frequency range, resistivity, and so on, to develop more sophisticated temperature sensors. The progress in micro and nanoelectronics has led to the development of CMOS-based temperature sensors with excellent performance, but they suffer from large process variation and large power consumption due to high nonlinearity [17]. To overcome the problem of nonlinearity, various ceramic nanocomposites, such as $BaTiO_3$ [18], [19], $SrTiO_3$ [20], $BaTiO_3$–$BaSnO_3$ [21], and so on, are used for fabrication of temperature sensors but still, they are not sufficient to achieve good temperature stability, sensitivity, and reliability [11], [12], [13]. Therefore, lead-based perovskite systems such as $Pb(Zr_{1-x}Ti_x)O_3$, $Pb(Mg_{1/3}Nb_{2/3})O_3$, $PbTiO_3$, and so on are preferred due to their advantageous capacitive, ferroelectric and dielectric characteristics for the development of temperature sensors [22]. However, the toxic and hazardous effects of lead on both human health and the environment led to an emphasis on the fabrication of eco-friendly sensing materials for the design of temperature sensors.

The surge of interest in ferroelectric materials has triggered technological advancement in next-generation temperature sensor applications based on their naturally exhibited pyroelectric behavior. Bismuth ferrite [$BiFeO_3$ (BFO)] is a unique material that is potential of high interest for temperature sensors, but still, it is limited due to larger leakage current [23], [24]. In order to reduce the leakage current, and tangent loss with improved physical properties, the perovskite BFO compound is modified by substituting at both Bi (A-site) and/Fe (B-site). Thus, in this article, an eco-friendly transition metal (tantalum Ta^{5+}) doped bismuth-based electronic material $Bi(Fe_{2/3}Ta_{1/3})O_3$ has been synthesized and developed as a capacitive sensor that will be widely preferred in a broad range of applications due to their low fabrication cost, lower loss at a higher frequency, polarity independent voltage tenability, low-power consumption, and longer functional life.

This research aims to evaluate the synthesized material's potential as a ferroelectric capacitor by investigating its physical and electrical properties, including crystallographic structure, morphology, dielectric constant, impedance, leakage current, polarization, conductivity, and electric modulus. Section II focuses on sensor element structure, covering sensing material preparation, characterization, system operation, and integration of the capacitive sensor as an active low-pass filter (LPF). An active LPF, using the developed BFT component as a lumped capacitor, is designed in Section II to assess the material's feasibility as a temperature sensor. Section III demonstrates the material's suitability as a ferroelectric capacitive temperature sensor through an in-depth equivalent circuit model analysis and experimental validation, examining structural, morphological, and compositional aspects, dielectric and ferroelectric properties, leakage current, and impedance spectroscopy. This article concludes in Section IV by summarizing the key findings and their implications.
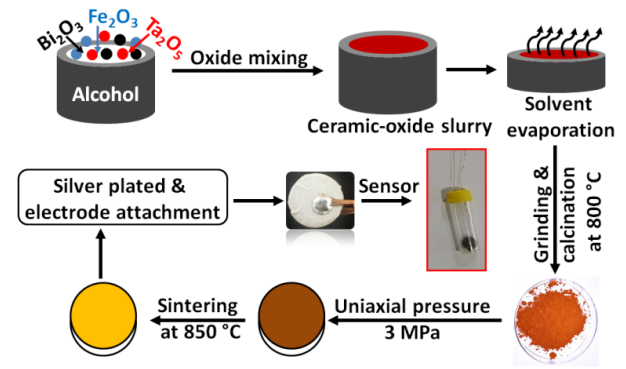

Fig. 1. BFT-based capacitive sensor fabrication process.

II. CAPACITIVE SENSOR ELEMENT FABRICATION

A. Sensing Material Preparation, Characterization, and Capacitive Sensor Fabrication

The processes involved in the design and fabrication of $Bi(Fe_{2/3}Ta_{1/3})O_3$ ferroelectric capacitive sensor have been elucidated in Fig. 1. The typical solid-state homogeneous oxide mixture technique has been adopted to obtain the ferroelectric capacitive component of the BFT [25]. To synthesize the proposed temperature sensor, highly pure (>99.5%) oxides, such as Bi_2O_3 (60.7%), $FeCO_3$ (20.12%), and Ta_2O_5 (19.18%) are mixed in suitable stoichiometric proportions. The chemical equation is balanced in accordance with the charge neutrality condition used for the fabrication of the BFT component. The synthesis of solid solutions follows this chemical reaction:

$$\frac{1}{2}Bi_2O_3 + \frac{3}{2}FeCO_3 + \frac{1}{6}Ta_2O_5 \rightarrow BiFe_{2/3}Ta_{1/3}O_3$$
$$+ \frac{2}{3}CO_2 \uparrow .$$
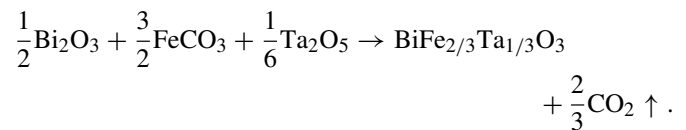
Ceramic oxide powders are ground in dry air followed by methanol in a wet atmosphere to obtain a solid solution of BFT and then the powder is calcined at 800 °C. Basic information about the formulation of solid solutions is identified with the help of an X-ray diffractometer tool (Rigaku Ultima IV, Japan). The calcined powders are ground again to prepare a fine powder. In the next stage, the powder is mixed with a binder (polyvinyl alcohol) and pressed into a disk-shaped pellet with 2 mm thickness and 10 mm diameter using a hydraulic press at a pressure of 3 MPa at room temperature. The prepared pellets are sintered at 850 °C for a duration of 8 h. The surface morphology and composition (real concentration of the compound) analysis are performed through a scanning electron microscope (JEOL Ltd., SEM) and an energy-dispersive X-ray pattern. The top and bottom areas of the sintered pellets are properly polished using emery papers, and the electrodes are engineered through a high-quality silver (Ag) metal paste, which usually tolerates relatively high temperatures. Copper (Cu) wires were attached to the silver electrodes as conducting wires for the measurement of the sensing characteristics. The ferroelectric BFT component, which is compressed between two silver electrodes, thus forms a capacitive structure that has been further used in an *RC* filter
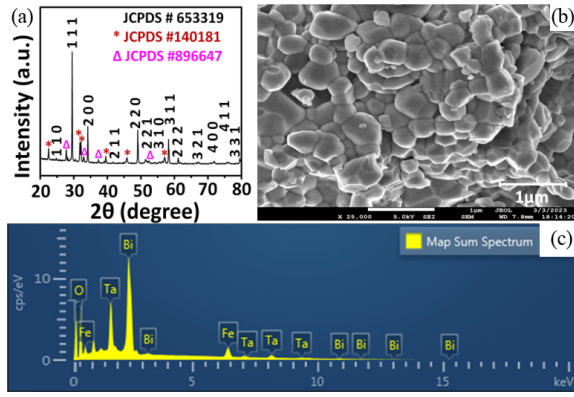
Fig. 2. (a) Indexed XRD pattern, (b) SEM image, and (c) EDX pattern of BFT sample.

Fig. 3. Mapping pattern of BFT specimen (a) Bi, (b) Ka, (c) Ta, and (d) Fe.

network (circuit containing a resistor-ferroelectric capacitor specimen) to verify its operation as a temperature sensor. By using a computer-controlled phase sensitive LCR meter N4L-PSM1735, the different temperature-dependent electrical properties (dielectric constant, phase angle, impedance, and tangent loss) are measured. The associated dielectric components, along with impedance, are measured for temperature ranges from 25 °C to 500 °C with frequencies from 1 kHz to 1 MHz with the help of an impedance analyzer.

B. Structural and Morphological Analysis

The room-temperature XRD patterns of the BFT material system are shown in Fig. 2(a). To collect basic information about the prepared BFT solid solution, the data has been analyzed using "Xpert" high score plus software. The spectrum shows that all of the distinct prominent peaks have been indexed with various (h, k, and l) planes. The well-defined sharp peaks of the XRD pattern reveal the polycrystalline nature of the sample. The Bragg angles associated with the XRD pattern's peak locations are matched to the constituent ingredients' preexisting JCPDS data files: $BiFeO_3$ (#140181), Bi_2O_3 (#653319), and $Bi_7Ta_3O_18$ (#896647). This may support the existence of the proposed material system.

The scanning electron microstructure of the compacted BFT pellet recorded at room temperature is shown in Fig. 2(b). On the basis of the micrograph, the existence of a polycrystalline microstructure of the compound can be identified as a result of several uniform but randomly distributed grains of various sizes on the entire sample surface. The EDX spectrum is illustrated in Fig. 2(c), which has been used to examine the elemental components and the purity of the chemical composition. Spectral analysis shows the existence of bismuth, iron, oxygen, tantalum, and no other foreign elements in the prepared sample. The uniform distribution of elements in the pellet can be well established from the mapping spectrum, as shown in Fig. 3.

C. Capacitive Temperature Sensor Operation

A capacitor is an electronic component consisting of two conducting plates that are separated by an insulating material. The sensing capacitance C_{ss} of the capacitive sensors can be
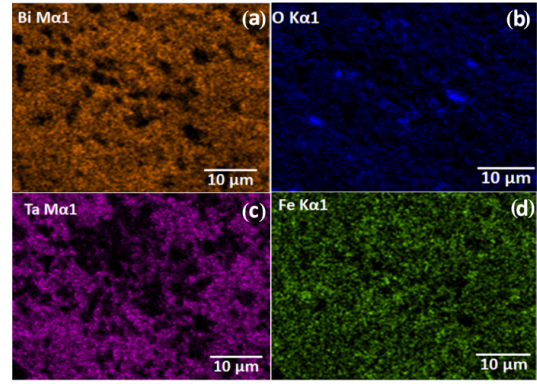
calculated as [26]

$$C_{ss} = \frac{\varepsilon_0 \varepsilon_r A}{d} \tag{1}$$

where A is the sensing area of the capacitor, ε_0 is the permittivity of the free space, ε_r is the relative dielectric constant of the sensing element, and d is the thickness of the sensing element. The temperature dependence capacitance $C_{ss,T}$ measured at temperature T can be modeled as

$$C_{ss,T} = C_{ss} + \beta \Delta T \tag{2}$$

where C_{ss} is the capacitance measured at room temperature T_0, and β is the temperature coefficient of the capacitance at T_0. ΔC_{ss} ($= C_{ss,T} - C_{ss}$) is the change in capacitance of the sensor with the change in temperature ($\Delta T = T - T_0$). From (2), it can be seen that there is a linear dependence of the temperature on the capacitance. The ε_r of the capacitor is a particularly important sensing parameter when designing temperature sensors since ferroelectric compounds possess a temperature sensitive ε_r. Specifically, the temperature-sensitive ε_r of a ferroelectric compound consists of two regions: above and below the transition temperature T_c. This article focuses on the development of a capacitive temperature sensor using a fabricated ferroelectric material (BFT) below T_c, with the intention of using it for low-power industrial applications.

D. Capacitive Sensor as an Active LPF

The capacitive structure developed above has been embedded in an LPF network to observe the temperature-sensing behavior of the sensing element. The circuit includes a single ferroelectric temperature-sensitive capacitor (BFT) and three resistors (R_{11}, R_{22}, and R_{33}), along with an operational amplifier (op-amp). The input voltage (V_{in}) is fed to the series combination of resistor R_{33} and the sensing capacitor (C_{ss}), while the output voltage (V_o) is taken only through the capacitor. The LPF contains amplifiers to increase signal strength, allowing only the lower frequency range of signals (from 0 Hz to the cutoff frequency f_c) to pass through, while attenuating the higher frequency range. The designed circuit structure is shown in Fig. 4.

To form a complete resistor–capacitor (RC) active LPF network, the fabricated ferroelectric capacitive sensor is combined
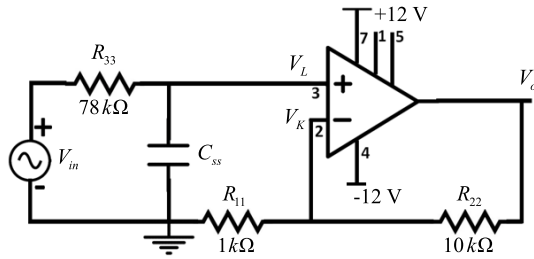
Fig. 4. Equivalent model of the temperature sensor circuit.

with resistors and an op-amp. The reactance of C_{ss} at lower frequencies is higher compared to the resistance value of R_{33}, resulting in a lower voltage drop across R_{33} than the voltage across C_{ss}. However, at higher frequencies, the opposite is true, with the reactance of C_{ss} being lower than the resistance of R_{33}. Consequently, the LPF blocks higher frequency signals, while allowing lower frequency signals to pass through. The voltage across C_{ss} is calculated as

$$V_o = \frac{X_c}{Z} V_{in}. \tag{3}$$

The capacitive reactance of C_{ss} can be denoted as X_c and can be represented as $X_c = 1/2\pi f C_{ss}$. As shown in Fig. 4, the impedance of the input RC network can be denoted as $Z \ (= (R^2 + X_c^2)^{1/2})$ by considering $R_{33} = R$. As shown in Fig. 4, V_L and V_K are op-amp noninverting and inverting terminal voltages, while V_o denotes the output voltage and can be represented as

$$V_K = \frac{R_{11}}{R_{11} + R_{22}} V_o; \quad V_L = \frac{1}{1 + RC_{ss}s} V_{in}. \tag{4}$$

Now, the dc gain $A(s)$ of the op-amp can be represented as

$$A(s) = \frac{V_o}{(V_L - V_K)} = \frac{A_{fg}}{1 + \frac{s}{\omega_d}} \tag{5}$$

where $s = j\omega$ is the Laplace operator with $\omega \ (= 2\pi f)$ as angular frequency. A_{fg} is the passband gain of the filter and can be further represented as

$$A_{fg} = 1 + \frac{R_{22}}{R_{11}}. \tag{6}$$

Considering a dominant pole at $s = -\omega_d$, i.e., $\omega > \omega_d$, $A(s)$ from (5) can be further modeled as

$$A(s) \approx \frac{A_{fg}\omega_d}{s} \approx \frac{\omega_g}{s} \tag{7}$$

where ω_g is the unity gain frequency. From (9) and (11), V_L can be written as

$$V_L = \left(\frac{R_{11}}{R_{11} + R_{22}} + \frac{s}{\omega_g} \right) V_o. \tag{8}$$

By solving (8) and (12), the inverting terminal voltage can be equated to

$$V_L = \left(\frac{R_{11}}{R_{11} + R_{22}} + \frac{s}{\omega_g} \right) V_o = \frac{1}{1 + RC_{ss}s} V_{in}. \tag{9}$$

At the cutoff frequency (f_c), the real part of (9) is zero and in the ideal case ω_g tends to infinity. Now, the gain A_{ss} of the active LPF can be obtained as

$$A_{ss} = \frac{V_o}{V_{in}} = \frac{A_{fg}}{\sqrt{1 + k_f^2}}. \tag{10}$$

The variable $k_f \ (= f/f_c)$ is the relationship between the input signal frequency (f) and the cutoff frequency (f_c). For $0 < f < f_c$, the gain is $A_{ss} = A_{fg}/\sqrt{2} = 0.707 \ A_{fg}$ at the cutoff point and above it, with increasing frequency, it decreases at a constant rate. The voltage gain magnitude calculated in (dB) is given as

$$A_{ss}(dB) = 20\log_{10}\left(\frac{V_o}{V_{in}} \right) = 20\log_{10}\left(\frac{A_{fg}}{\sqrt{1 + k_f^2}} \right). \tag{11}$$

The 3-dB point for the above can be calculated as

$$A_{ss}|_{-3\,dB} = 20\log_{10}\left(\frac{V_o}{\sqrt{2}V_{in}} \right) = 20\log_{10}\left(0.707\frac{A_{fg}}{\sqrt{1 + k_f^2}} \right). \tag{12}$$

Now, the cutoff frequency (f_c) of the RC network can be defined by the frequency at which the capacitive reactance is equal to the resistance and can be written as

$$f_c = \frac{1}{2\pi RC_{ss}}. \tag{13}$$

Taking into account the temperature dependence of the capacitor, the cutoff frequency $f_{c,T}$ can be represented as [27]

$$f_{c,T} = \frac{1}{2\pi RC_{ss,T}}. \tag{14}$$

By putting $C_{ss,T}$ from (2), $f_{c,T}$ can be modified as

$$f_{c,T} = \frac{1}{2\pi R \left(C_{ss} + \beta\Delta T \right)}. \tag{15}$$

The relative change in the cutoff frequency for a temperature variation from T_0 to T is given by

$$\frac{f_{c,T} - f_c}{f_c} = \frac{-\beta\Delta T}{C_{ss} + \beta\Delta T} \tag{16}$$

where f_c is the frequency at T_0. The cutoff frequency (f_c) of the active LPF circuit is obtained at the -3-dB point of maximum gain (A_{ss}). To investigate the effect of operating frequency on the gain (in dB) level at the output of the system, simulation measurements were carried out using Multisim v10.1, as shown in Fig. 5(a). The simulated cutoff frequency was found to be 29.33 kHz.

To study the relationship between capacitance and cutoff frequency (f_c) with temperature, experiments were conducted at 25 °C, 50 °C, and 100 °C. At room temperature (i.e., 25 °C), the sensor capacitance C_{ss} was measured to be 69 pF. With a resistance (R) value of 70 kΩ, the experimental f_c was found to be 26.36 kHz. It was observed that as the temperature increased, the sensor capacitance increased and for the same resistance value, the cutoff frequency decreased to 25.63 and 25 kHz, respectively. The comparison of the cutoff
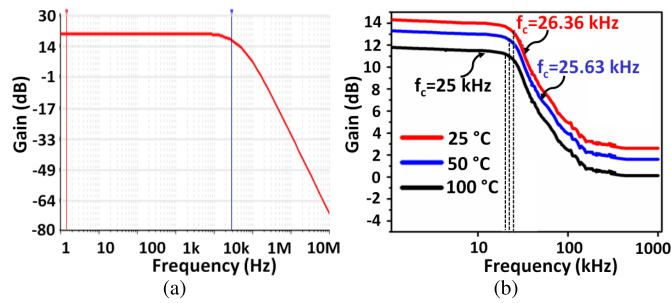
Fig. 5. Cutoff frequency (a) simulation study and (b) experimental study at different temperatures.
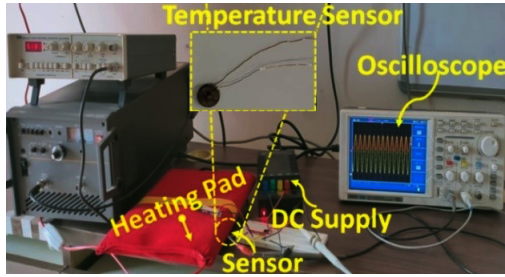

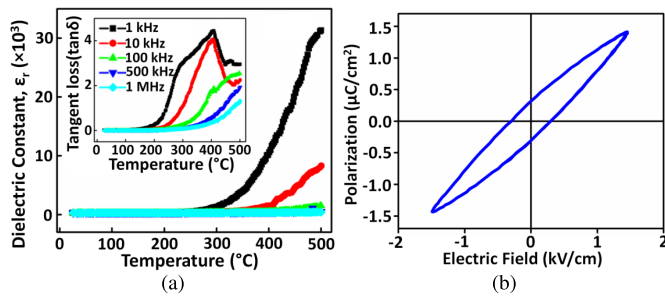Fig. 6. Experimental setup demonstration.

Fig. 7. Temperature-dependent (a) dielectric constant, (b) tangent loss at selected frequency, and (c) P–E hysteresis loop of BFT capacitor.

frequency (f_c) with the temperature at 25 °C, 50 °C, and 100 °C is shown in Fig. 5(b). It can be seen that as the temperature increases, the cutoff frequency decreases, as both the cutoff frequency and capacitance are inversely related. The above analysis indicates that the theoretical (29.58 kHz), simulated (29.33 kHz), and experimental (26.36 kHz) cutoff frequency output results at 25 °C for the given active LPF circuit were found to be similar. Therefore, the designed temperature sensor can be effectively used for lower temperature sensing applications.

III. RESULTS AND DISCUSSIONS

A. Experimental Prototype Description

To investigate the temperature-sensing capability of the fabricated electronic component, a simulation measurement and experimental setup have been built as shown in Fig. 6.

B. Ferroelectric Property Analysis

1) Dielectric Study: The temperature-dependent dielectric constant (ε_r) and the tangent loss (tan δ) are shown in Fig. 7(a)
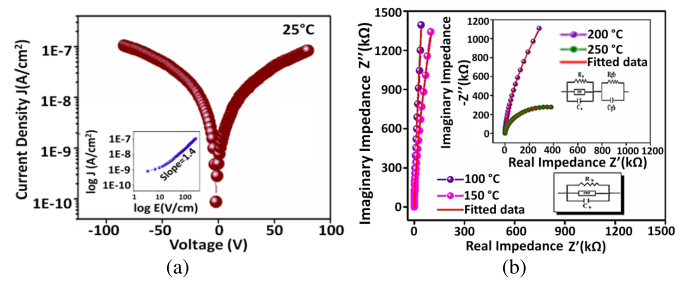

Fig. 8. (a) Leakage current density of BFT capacitor and (b) frequency-dependent Z' versus Z'' plot.

at selected frequency. According to Wagner and Koop's model [28], the dielectric consists of very low conducting grain boundaries (large resistance value) and conducting grains (bulks). Hence, the accumulation of electrons occurs at boundaries that create space-charge polarization. Therefore, it can be seen that at a lower frequency, the value of ε_r is high. At higher frequencies, the dipoles are not fast enough to align themselves with the applied electric field, so the polarization effect slowly ceases (except electronic) and decreases ε_r in value with frequency. The tan δ follows similar characteristics with temperature as ε_r. The decrease in loss with an increase in frequency may arise as a result of the inertia of oxygen vacancies. At high temperatures, peaks are observed that move to the higher range of temperature with a rise in frequency, which confirms that the sample possesses relaxation behavior.

2) Hysteresis Loop (Ferroelectric Property): The hysteresis behavior of the sensor component is investigated using polarization (P) with an electric field (E) loop tracer (Marine India Electricals Pvt. Ltd.), as shown in Fig. 7(b). The $P–E$ loop is obtained at a frequency of 50 kHz with a resistor and a capacitor value of 1 kΩ and 0.47 μF, respectively, which confirms the presence of a ferroelectric property in the specimen. The loop of the material at room temperature exhibits a remnant polarization (P_r) of 0.42 μC/cm^2 in a lower electric field, which has an effect on decreasing the loss and leakage current. It is the main need for the design of a ferroelectric-based temperature sensor.

3) Leakage Current Characteristics: The current density–voltage characteristic, as illustrated in Fig. 8(a), is helpful to recognize the conduction phenomenon of the BFT capacitor sample (leakage current measured using the Keithley electrometer model 6517B). The component at room temperature shows a lower leakage current after it is doped with tantalum. The leakage current density of the ceramic capacitor at 100 kV/cm is observed to be 1.4 × 10^{-8} A/cm^2. It can be seen that the plot is not linear (i.e., the rise in current density with the increase in electric field), suggesting the presence of nonohmic characteristics in the system. The leakage current mechanism can be well illustrated with the logarithmic plot of $J–E$, as shown in the inset of Fig. 8(a). The nature is identified to be linear at the lower electric field. From this current density fitting, the slope of the BFT sample is found to be the same, which is in accordance with the space-charge-limited-conduction behavior of the ferroelectric BFT [28].

TABLE I
VALUES OF BULK RESISTANCE (R_g) AND GRAIN BOUNDARY
RESISTANCE (R_{gb}) OBTAINED FROM THE ARC
INTERCEPTS ON THE REAL AXIS

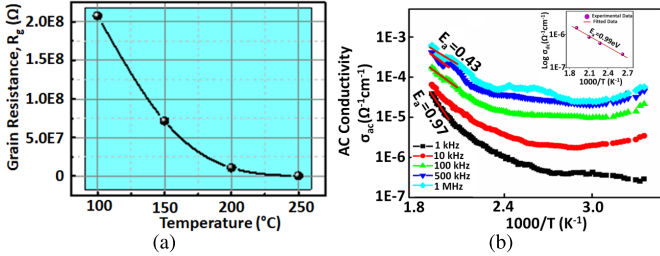| T (°C)	R_g (MΩ)	C_g (pF)	CPE (nF)	R_{gb} (kΩ)	C_{gb} (nF)
100	208.00	0.0903	0.0443	-	-
150	71.55	110.1	0.1268	-	-
200	10.9	108.9	0.1196	2.704	5.723
250	0.6689	110	2.363	16.46	6.377

Fig. 9. (a) Variation of grain resistance of BFT specimen with temperature and (b) σ_{ac} versus T^{-1} at different f.

Fig. 10. Frequency-dependent (a) M' and M'' graph of BFT. (b) Variation of the M'' and Z''.

4) Impedance Spectroscopy: Impedance spectroscopy is an influential approach to dissociating the contribution of the grain and the grain boundary effect to the total conductivity of the compound. The real (Z') and imaginary (Z'') part of the impedance Z is described by the following relation:

$$Z' = \frac{R}{1 + (\omega\tau)^2} \quad \text{and} \quad Z'' = \frac{\omega R\tau}{1 + (\omega\tau)^2}. \quad (17)$$

Fig. 8(b) illustrates the plot of Z' versus Z'' (Nyquist diagram) at various temperatures over a wider frequency range. With an increase in temperature, the appearance of semicircles characterizes the impedance. In the Nyquist plots, between the temperature range of (100 °C–150 °C) the occurrence of a single semicircular arc specifies that electrical conduction at that particular temperature range is due to the effect of grain that is modeled by an R–Q–C circuit connected in parallel. At (200 °C–250 °C), the appearance of two semicircular arcs can be marked, indicating that conduction is due to both grain and grain boundary effects modeled by the R–Q–C and RC networks. Table I shows the values of the bulk resistance (R_g) and the grain boundary resistance (R_{gb}) obtained from the arc intercepts on the real axis. The values of R_g decrease with the increase in temperature that can be observed from Fig. 9(a), indicating the declining nature of the grain resistive behavior of the compound.

5) Conductivity Analysis: Both the ac conductivity (σ_{ac}) and dc conductivity (σ_{dc}) part of the electric field contribute toward the total conductivity (σ_{ss}) of the sample [29]. The temperature-dependent conductivity property of the BFT compound is delineated through σ_{ac} versus T^{-1} curves plotted at different frequencies, as shown in Fig. 9(b)

$$\sigma_{ss} = \sigma_{dc} + \sigma_{ac}. \quad (18)$$

The dielectric data obtained from the LCR meter is used to calculate the ac conductivity value using the following relation:

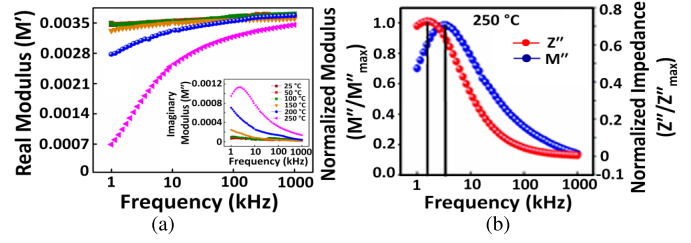$$\sigma_{ac} = \omega\varepsilon_r\varepsilon_0 \tan\delta. \quad (19)$$

The dc conductivity σ_{dc} is measured by extrapolating the conductivity spectrum in the lower region of the frequency. The conductivity spectra follow the Arrhenius relation as:

$$\sigma_{dc} = \sigma_0 \exp\left(-E_a/kT\right) \quad (20)$$

where k is Boltzmann's constant (1.38×10^{-23} J/K), σ_0 is the pre-exponential factor, and E_a is the activation energy. The linear fitting of the plot helps to calculate E_a which decreases at a higher frequency due to the migration of oxygen vacancy. This clarifies the mechanism of the thermally activated relaxation process of the BFT sample. The linear fitting data of the plot show a higher value of E_a, i.e., 0.99 eV, indicating that the conduction mechanism can be activated with a small amount of energy.

6) Modulus Analysis: The relaxation mechanism in materials and the phenomenon of electrical transport can be an insight from the complex electric modulus technique. Fig. 10(a) shows the characteristics of a frequency-dependent complex modulus real (M') and imaginary part (M'') at various temperatures (25 °C–250 °C). In the compound at lower frequencies, M' moves toward zero with monotonic dispersion, signifying the absence or negligibly small contribution of the electrode polarization effect. Due to the suppression of space-charge polarization, a similar value of M' can be observed at various temperatures at a higher frequency. The graph shows that with increasing frequency, M'' increases and reaches maximum (M''_{max}), which confirms the existence of relaxation in the sample. A distinct peak can be detected in the M'' versus frequency plot related to a relaxation process.

Fig. 10(b) shows the variation of M'' and Z'' with frequency at 250 °C. The non-Debye type of characteristics can be indicated by noticing a smaller gap between the two peaks (Z'' and M'') in the specimen. As at a common frequency, the peak of both spectrums does not coincide; therefore, a shorter range motion of charge carriers is indicated. The relaxation time versus temperature is shown in Fig. 11(a). The relaxation time roughly obeys an exponential decline with the temperature that may arise as in higher temperature, the electron scattering is more frequent.

C. Temperature Sensor Performance Analysis

1) Temperature-Dependent Capacitance, Linearity, and Sensitivity Analysis: To realize the linearity characteristics of the manufactured temperature sensor, the capacitive response of the sensor in the temperature range of 25 °C–450 °C is analyzed in Fig. 11(b). The experimental analysis of the data
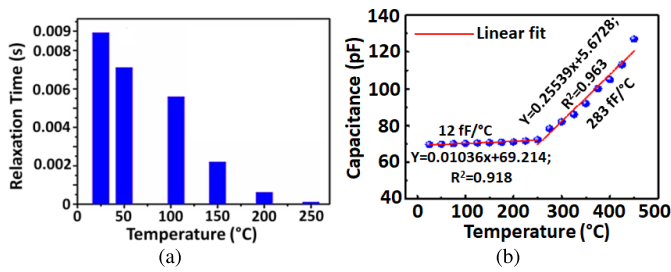
Fig. 11. (a) Temperature-dependent relaxation plot of BFT capacitive sensor. (b) Temperature-dependent capacitance response of BFT temperature sensor.

Fig. 12. Response and recovery behavior of the BFT temperature sensor for (a) one cycle and (b) seven cycles.

obtained confirmed the excellent linearity ($Y = 0.01036X + 69.214$; $R^2 = 0.91837$) within the temperature 25 °C–250 °C range and ($Y = 0.25539X + 5.6728$; $R^2 = 0.96278$) in 250 °C–450 °C. The plot shows that the capacitance almost linearly increases with temperature and for 225 °C change in temperature the capacitance changes by 3.76%. The dielectric constant increases with temperature $<T_c$, which may be due to the change in transverse and longitudinal optical phonons with temperature, the so-called Lydanne–Sachs–Teller relation, which results in an increase in capacitance value [30]. To understand the effect of capacitance on the variation of temperature, the sensor sensitivity (S) is calculated as follows:

$$S = \frac{\Delta C_{\text{ss}}}{\Delta T} = \beta - \frac{\beta_\varepsilon \varepsilon_r}{1 + \varepsilon_r \frac{\partial \ln(\beta)}{\partial \ln(T)}} \quad (21)$$

where β_ε is the temperature coefficient of the dielectric constant, ε_r is the dielectric constant at the reference temperature, and $(\partial \ln(\beta))/(\partial \ln(T))$ is the temperature coefficient of capacitance at temperature T. The sensor sensitivity is observed to be relatively high 283 fF/°C at elevated temperature (>250 °C) and 12 fF/°C at lower temperature (up to 250 °C). The maximum sensitivity is relatively larger than the other available research outcomes, as mentioned in Table II. Hence, the designed temperature sensor is appropriate for higher temperature sensing applications. Furthermore, the resolution of the BFT-based temperature sensor has been delineated. The temperature sensor resolution is given by: $1/S = 1/(283 \text{ fF/°C}) = 3.53$ °C/fF. By using the "Arduino Uno" microcontroller, the temperature resolution is observed to be 3.53 for a capacitance resolution of 0.138 fF and sensitivity of 283 fF/°C. The straight line fitting in the graph gives the sensor sensitivity to be 0.016 pF/°C at a lower temperature (up to 240 °C) and (inset) shows 0.28 pF/°C at higher temperature (>240 °C).

2) Response and Recovery Times, Repeatability, Hysteresis, and Stability Analyses: Response and recovery time play an important role in determining sensor performance for real-time implementation. Two separate chambers (25 °C and 450 °C) are used for the determination of response and recovery time of the developed sensor, as illustrated in Fig. 12. The time is taken by the temperature sensor to achieve 10%–90% of the saturated capacitance value with increasing temperature from 25 °C to 450 °C is determined as the response time. The time needed to alter the original capacitance response from 90% to 10% with the decrease in temperature from 25 °C to 450 °C
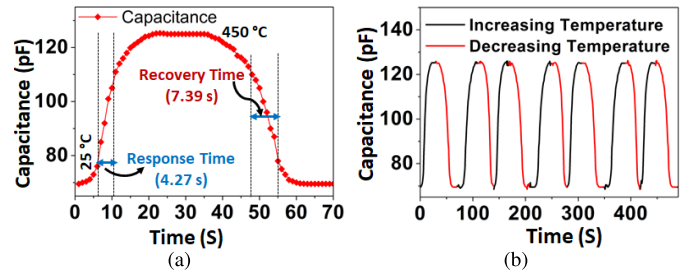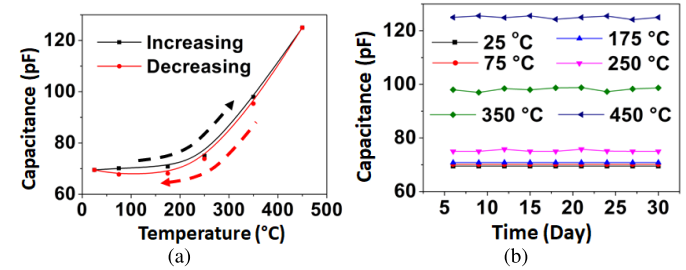

Fig. 13. (a) Hysteresis performance and (b) long-term stability response of the BFT temperature sensor.

TABLE II
COMPARISON OF EXISTING CAPACITIVE TEMPERATURES

Sensor	C_{ss}, (pF)	S (fF/°C)	Ref.
Capacitive	69.2	7	[31]
Capacitive	8.2	50.7	[32]
Capacitive	0.3	1	[33]
Capacitive	0.6	20	[34]
Capacitive	75.918	156	[35]
Capacitive	40.25	32.45	[36]
Capacitive	69	280	Proposed

is known as the recovery time. The response and recovery time of the developed sensor are 4.27 and 7.39 s, respectively, as shown in Fig. 12(a). The response and recovery time obtained from the capacitive temperature sensor is relatively faster than the other research outcomes available, as mentioned in Table II. A reliable sensor response is essential for long-term use. So, the repeatability of the sensor is tested by exposing them to an uninterrupted temperature cycle changing from 25 °C to 450 °C. As indicated in Fig. 12(b), the sensor shows remarkable repeatability.

As for response and recovery time, hysteresis is also an important parameter to measure sensor performance. The deviation in the sensing response due to increase and decrease in temperature is known as hysteresis. The hysteresis value of the sensor is determined by interchanging the sensor in different temperature environments (25 °C–450 °C) and then relocating back. The hysteresis response of the sensor is shown in Fig. 13(a). The maximum hysteresis H_{max} can be calculated as

$$H_{\text{max}} = \frac{C_{175\uparrow} - C_{175\downarrow}}{T_{\text{span}}} \quad (22)$$

where $C_{175\uparrow}$ and $C_{175\downarrow}$ are the values of capacitance at °C in increasing and decreasing temperature, respectively, at the entire temperature span of T_{span}. The hysteresis is found to be 1.10% which indicates a relatively low hysteresis response

that is a unique feature of the developed temperature sensor. To analyze the long-term stability, the developed temperature sensor is placed in various temperature environments for a period of 30 days. The capacitance of the sensor is recorded every three days at various temperature conditions, as shown in Fig. 13(b). There is a negligible variation of capacitance observed over 30 days, which confirms the long-duration stability of the sensor.

IV. CONCLUSION

A novel capacitive temperature sensor has been designed using the ferroelectric temperature-sensing element $Bi(Fe_{2/3}Ta_{1/3})O_3$, making it suitable for monitoring temperature in diverse functional applications. The physical (structural, morphological, and compositional) and electrical (dielectric, conductive, impedance, ferroelectric, and capacitive) properties of the BFT solid solution have been thoroughly investigated to establish its suitability as a capacitive sensor component. The temperature sensing capability of the fabricated BFT capacitor was analyzed by incorporating it into an active filter network, and its performance was characterized experimentally. Temperature changes were measured by monitoring variations in the cutoff frequency of the active LPF. The enhanced sensitivity, good linearity, rapid response and recovery times, relatively low hysteresis, and excellent stability demonstrated by the sensor make it a promising candidate for various industrial and biomedical applications.

ACKNOWLEDGMENT

REFERENCES

[1] A. Žužić, A. Ressler, and J. Macan, "Perovskite oxides as active materials in novel alternatives to well-known technologies: A review," *Ceram. Int.*, vol. 48, no. 19, pp. 27240–27261, Oct. 2022.

[2] J. F. Scott, "Applications of modern ferroelectrics," *Science*, vol. 315, no. 5814, pp. 954–959, Feb. 2007.

[3] D. Damjanovic, P. Muralt, and N. Setter, "Ferroelectric sensors," *IEEE Sensors J.*, vol. 1, no. 3, pp. 191–206, Oct. 2001.

[4] P. Muralt, "Ferroelectric thin films for micro-sensors and actuators: A review," *J. Micromech. Microeng.*, vol. 10, no. 2, pp. 136–146, Jun. 2000.

[5] S.-H. Shin, D. H. Park, J.-Y. Jung, M. H. Lee, and J. Nah, "Ferroelectric zinc oxide nanowire embedded flexible sensor for motion and temperature sensing," *ACS Appl. Mater. Interfaces*, vol. 9, no. 11, pp. 9233–9238, Mar. 2017.

[6] S. Gupta, L. Lorenzelli, and R. Dahiya, "Multifunctional flexible PVDF-TrFE/BaTiO3 based tactile sensor for touch and temperature monitoring," in *Proc. IEEE SENSORS*, Oct./Nov. 2017, pp. 1–3.

[7] Y. Lee et al., "Flexible ferroelectric sensors with ultrahigh pressure sensitivity and linear response over exceptionally broad pressure range," *ACS Nano*, vol. 12, no. 4, pp. 4045–4054, Apr. 2018.

[8] J. Lenz and A. S. Edelstein, "Magnetic sensors and their applications," *IEEE Sensors J.*, vol. 6, no. 3, pp. 631–649, Jun. 2006.

[9] S. C. Lai, K. Yao, Y. F. Chen, L. Zhang, and Y.-F. Lim, "A photovoltaic UV sensor with a ferroelectric thin film on transparent substrate," *IEEE Electron Device Lett.*, vol. 34, no. 11, pp. 1427–1429, Nov. 2013.

[10] A. M. Ahmed and A. Mehaney, "Novel design of wide temperature ranges sensor based on Tamm state in a pyroelectric photonic crystal with high sensitivity," *Phys. E, Low-Dimensional Syst. Nanostruct.*, vol. 125, Jan. 2021, Art. no. 114387.

[11] B. Ando, P. Giannone, S. Graziani, and N. Pitrone, "Characterization of the dielectric and pyroelectric properties of ferroelectric material," *IEEE Trans. Instrum. Meas.*, vol. 57, no. 9, pp. 1939–1948, Sep. 2008.

[12] M. K. Law, A. Bermak, and H. C. Luong, "A sub-μW embedded CMOS temperature sensor for RFID food monitoring application," *IEEE J. Solid-State Circuits*, vol. 45, no. 6, pp. 1246–1255, Jun. 2010.

[13] A. Davidson, A. Buis, and I. Glesk, "Toward novel wearable pyroelectric temperature sensor for medical applications," *IEEE Sensors J.*, vol. 17, no. 20, pp. 6682–6689, Oct. 2017.

[14] H. Li, C. R. Bowen, and Y. Yang, "Phase transition enhanced pyroelectric nanogenerators for self-powered temperature sensors," *Nano Energy*, vol. 102, 2022, Art. no. 107657.

[15] A. Bakker, J. H. Huijsing, and J. Huijsing, *High-Accuracy CMOS Smart Temperature Sensors*, vol. 595. New York, NY, USA: Springer, 2000.

[16] C. Chiang and F. Chang, "Design of a calibrated temperature difference sensor transducer for monitoring environmental temperature difference applications," *IEEE Sensors J.*, vol. 16, no. 4, pp. 1038–1043, Feb. 2016.

[17] M. A. Pertijs, A. Niederkorn, X. Ma, B. McKillop, A. Bakker, and J. Huijsing, "A CMOS smart temperature sensor with a 3σ inaccuracy of ± 0.5 °C from -50 °C to 120 °C," *IEEE J. Solid-State Circuits*, vol. 40, no. 2, pp. 454–461, Mar. 2005.

[18] R. Muhammad, Y. Iqbal, and I. M. Reaney, "BaTiO3–Bi(Mg2/3Nb1/3)O3 ceramics for high-temperature capacitor applications," *J. Amer. Ceram. Soc.*, vol. 99, no. 6, pp. 2089–2095, 2016.

[19] S. N. Das, S. K. Pardhan, S. Bhuyan, S. Sahoo, R. N. P. Choudhary, and M. N. Goswami, "Dielectric and impedance characteristics of nickel-modified BiFeO3-BaTiO3 electronic compound," *J. Electron. Mater.*, vol. 47, no. 1, pp. 843–854, Jan. 2018.

[20] Y. Ji, K. Zhang, Z. L. Wang, and Y. Yang, "Piezo–pyro–photoelectric effects induced coupling enhancement of charge quantity in BaTiO3 materials for simultaneously scavenging light and vibration energies," *Energy, Environ. Sci.*, vol. 12, no. 4, pp. 1231–1240, 2019.

[21] K. Shimada, H. Takashima, R. Wang, B. Prijamboedi, N. Miura, and M. Itoh, "Capacitance temperature sensor using ferroelectric (Sr0.95Ca0.05)TiO3 perovskite," *Ferroelectrics*, vol. 331, no. 1, pp. 141–145, Mar. 2006.

[22] Z. Zhigang and Z. Gang, "BTS: A new ferroelectric for multifunctional sensors," *Ferroelectrics*, vol. 101, no. 1, pp. 43–54, Jan. 1990.

[23] S. K. Samal, S. Halder, M. K. Mallick, R. N. P. Choudhary, and S. Bhuyan, "Frequency-and temperature-dependent dielectric features of multi-component electronic material: (Pb0.8Dy0.1Bi0.1)(Fe0.2Ti0.8)O3," *Appl. Phys. A, Solids Surf.*, vol. 126, no. 5, p. 377, May 2020.

[24] S. Halder, S. Bhuyan, and R. N. P. Choudhary, "Structural, dielectric and electrical properties of bismuth magnesium tantalate electronic system," *J. Magnesium Alloys*, vol. 7, no. 4, pp. 628–636, Dec. 2019.

[25] S. Das, S. Pradhan, D. Kar, S. Bhuyan, and R. Choudhary, "Excitation performance of fabricated PMN–BFO relaxor through electric field," *J. Mater. Sci., Mater. Electron.*, vol. 29, no. 11, pp. 9375–9379, 2018.

[26] S. Leppaevuori, P. Niemelä, T. Piila, and A. Uusimäki, "Miniature frequency-output temperature transmitter based on a ceramic capacitive sensor," *Sens. Actuators*, vol. 4, pp. 573–580, Jan. 1983.

[27] S. Pactitis, *Active Filters: Theory and Design*. Boca Raton, FL, USA: CRC Press, 2018.

[28] C. G. Koops, "On the dispersion of resistivity and dielectric constant of some semiconductors at audiofrequencies," *Phys. Rev.*, vol. 83, no. 1, pp. 121–124, Jul. 1951.

[29] S. Halder et al., "Structural, morphological, dielectric and impedance spectroscopy of lead-free Bi(Zn2/3Ta1/3)O3 electronic material," *Appl. Phys. A, Solids Surf.*, vol. 123, no. 12, pp. 1–8, Dec. 2017.

[30] W. Cochran, "Crystal stability and the theory of ferroelectricity," *Adv. Phys.*, vol. 9, no. 36, pp. 387–423, Oct. 1960.

[31] H.-Y. Ma, Q.-A. Huang, M. Qin, and T. Lu, "A micromachined silicon capacitive temperature sensor for wide temperature range applications," *J. Micromech. Microeng.*, vol. 20, no. 5, May 2010, Art. no. 055036.

[32] Q.-Y. Ren, L.-F. Wang, J.-Q. Huang, C. Zhang, and Q.-A. Huang, "A novel capacitive temperature sensor for a lab-on-a-chip system," in *Proc. IEEE SENSORS*, Nov. 2014, pp. 436–439.

[33] L. Toygur, A. Patil, J. Guo, X. Yu, and S. Garverick, "A 300 °C, SOI transimpedance amplifier with application to capacitive temperature sensing," in *Proc. IEEE SENSORS*, Oct. 2012, pp. 1–4.

[34] M. M. Othayq, N. Giganti, and M. Shavezipur, "Development of capacitive temperature sensors with high sensitivity using a multiuser polycrystalline silicon process," *Microelectron. Eng.*, vol. 226, Apr. 2020, Art. no. 111287.

[35] U. Salmaz, T. Islam, and S. Sohail, "A novel linear capacitive temperature sensor using polydimethylsiloxane," *IEEE Trans. Instrum. Meas.*, vol. 69, no. 10, pp. 7887–7894, Oct. 2020.

[36] Q.-Y. Ren, L.-F. Wang, and Q.-A. Huang, "Parallel capacitive temperature micro-sensor for passive wireless sensing applications," *Electron. Lett.*, vol. 52, no. 15, pp. 1345–1347, Jul. 2016.

Sarbasri Halder received the B.Tech. degree in electronics and communication engineering from the Biju Patnaik University of Technology, Rourkela, Odisha, India, in 2014, and the M.Tech. and Ph.D. degrees in microelectronics from the Department of Electronics and Communication Engineering, Siksha 'O' Anusandhan (Deemed to be University), Bhubaneswar, Odisha, in 2017 and 2021, respectively.

She is currently a Research Associate with Siksha 'O' Anusandhan (Deemed to be University). Her research interest includes electronic sensors, signal conditioning circuit designs, electronic device designs, and circuit simulation.

Satyanarayan Bhuyana (Member, IEEE) received the B.Sc. and M.Sc. degrees in physics from Utkal University, Bhubaneswar, Odisha, India, in 2002 and 2004, respectively, the M.Tech. degree in solid-state materials from the Department of Physics, Indian Institute of Technology Delhi, New Delhi, India, in 2006, and the Ph.D. degree from the School of Electrical and Electronic Engineering, Nanyang Technological University (NTU), Singapore, in 2011.

He was a Postdoctoral Research Fellow at the Department of Electrical and Computer Engineering, National University of Singapore (NUS), Singapore, from 2010 to 2011. He was a Scientist-I with the RF and Optical Department, Institute for Infocomm Research, A*STAR, Singapore, from 2011 to 2013. He is currently a Professor with the Department of Electrical and Electronics Engineering, Institute of Technical Education and Research (ITER), Siksha 'O' Anusandhan (Deemed to be University), Bhubaneswar. His current research involves fabrications and characterizations of solid-state electronic materials, devices, advanced smart ceramics sensor designs, piezoelectric actuators, wave electronics, electromagnetism, and the wireless energization of electrical and electronic devices.

Ashis Tripathy received the B.Tech. degree in applied electronics and instrumentation engineering from the Biju Patnaik University of Technology, Rourkela, Odisha, India, in 2007, the M.Tech. degree in electrical engineering from the Department of Electronics and Instrumentation Engineering, Jadavpur University, Kolkata, India, in 2010, and the Ph.D. (Hons.) degree in biomedical engineering from the University of Malaya, Kuala Lumpur, Malaysia, in 2017.

He is currently an Associate Professor with the School of Electronics Engineering (SENSE), Vellore Institute of Technology (VIT), Chennai, India. Prior to joining VIT, he was a Postdoctoral Investigator at the Center for MicroElectroMechanics Systems (CMEMS), University of Minho, Braga, Portugal. His current research involves fabrications and characterizations of micro/nanoelectronics devices, sensor and biosensor designs, flexible electronics, advanced smart ceramics nanocomposite synthesis and characterization, and biomedical applications.

Dr. Tripathy received the Award of Excellence for his Ph.D. degree.

Omar Al Zaabi (Member, IEEE) received the B.S., M.S., and Ph.D. degrees in electrical engineering from the Pennsylvania State University, University Park, State College, PA, USA, in 2012, 2014, and 2019, respectively.

He is currently an Assistant Professor with the Department of Electrical and Computer Engineering, Khalifa University, Abu Dhabi, United Arab Emirates, where he is also a member of the Advanced Power and Energy Center (APEC). His research interests include power electronics, renewable energy integration, and electromagnetic and its application to electrified transportation.

Biswaranjan Swain received the B.Tech. degree in applied electronics and instrumentation engineering and the M.Tech. degree in VLSI and embedded system designs from the Department of Electronics and Communication Engineering, Biju Patnaik University of Technology, Rourkela, Odisha, India, in 2007 and 2010, respectively, and the Ph.D. degree in electronics and communication engineering from Siksha 'O' Anusandhan (Deemed to be University), Bhubaneswar, Odisha, in 2018.

He is currently an Associate Professor with the Center for Internet of Things (CIOT), Siksha 'O' Anusandhan (Deemed to be University). His current research interests include embedded machine learning, wireless excitation of electronic sensors and actuators, low-power embedded system designs, fabrications, and characterizations of electronic devices, sensor designs, and biomedical electronics circuit designs.

Utkal Ranjan Muduli (Senior Member, IEEE) received the B.Tech. degree in electrical and electronics engineering from the Biju Patnaik University of Technology, Rourkela, India, in 2011, the M.Tech. degree in electrical engineering from the Indian Institute of Technology Gandhinagar, Gandhinagar, India, in 2014, and the Ph.D. degree in electrical engineering from the Indian Institute of Technology Patna, Patna, India, in 2022.

He was a Visiting Scholar and a Research Associate with the Department of Electrical Engineering and Computer Science, Khalifa University, Abu Dhabi, United Arab Emirates, in 2019 and 2021, respectively, where he is currently a Postdoctoral Research Fellow. His research interests include modulation strategies for multiphase motor drives, matrix converters and their control, battery power management, and wireless power transfer.

Dr. Muduli was a recipient of the 2022 IEEE Outstanding Paper Award for the IEEE TRANSACTIONS ON INDUSTRIAL ELECTRONICS.